Porous carbon nanofibers derived from low-softening-point coal pitch towards all-carbon potassium ion hybrid capacitors

Guang-Yuan Wang, Xiao-Hong Wang, Jin-Feng Sun* , Ya-Min Zhang,
Lin-Rui Hou* , Chang-Zhou Yuan*

Abstract Potassium ion hybrid capacitors (PIHC) have promising applications in medium and large-scale energy storage systems due to their high energy/power density, abundant potassium resource and low cost. However, the slow kinetics of battery-type anodes originating from the large-size K^+ results in a mismatch between the two electrodes, rendering the modest energy density of PIHC. Herein, we first develop an electrospinning strategy to successfully synthesize fibrous precursor by using the HNO_3 pre-oxidized low-softening-point coal pitch as the low-cost raw material. With further carbonization or KOH activation, the two types of carbon nanofibers (CNF) are fabricated as anode and cathode materials, respectively, towards the dual-carbon PIHC devices. Thanks to its three-dimensional interconnected porous conducting network and large layer spacing, the resulted CNF anode material is endowed with high reversible capacities, excellent rate and long cycle stability. Meanwhile, the activated CNF cathode with a large surface area of 2169 $m^2 \cdot g^{-1}$ exhibits excellent capacitive performance. A PIHC constructed with the two fibrous electrodes delivers an energy density of 110.0 $Wh \cdot kg^{-1}$ at 200.0 $W\ kg^{-1}$, along with a capacitance retention of 83.5% after 10,000 cycles at 1.0 $A \cdot g^{-1}$. The contribution here provides a cost-efficiency avenue and platform for advanced dual-carbon PIHC.

1 Introduction

As an emerging electrochemical energy storage system, metal ion (Li^+, Na^+, K^+, etc.) hybrid capacitors combined with the advantages of ion batteries and supercapacitors are expected to meet the medium and large-scale energy storage needs [1]. Among these, potassium ion hybrid capacitors (PIHC) are particularly valued for the following advantages. Firstly, metallic potassium is highly abundant and widely distributed in the earth's crust [2]. Secondly, among various metal/metal ion pairs, the redox potential of K/K^+ is the closest to that of Li/Li^+, which ensures the high energy density and high operating voltage of PIHC. Thirdly, K^+ has the lowest ion–solvent interaction energy and higher ionic conductivity in the electrolyte compared to other alkali ions (e.g., Li^+, Na^+) [3]. In addition, the weaker Lewis acidity of K^+ results in a smaller Stokes radius of the solvated ion, which facilitates the rapid diffusion of K^+ across the electrolyte/electrode interface in the electrolyte, resulting in a higher power density of the potassium-ion-based energy storage devices [4]. In view of the large radius of the K^+ (0.138 nm) [5], the large K^+ storage will cause rapid volume expansion and inevitably severe electrochemical pulverization [5, 6]. Moreover, the gap from the innate kinetic mismatch between anode and cathode involved in the sluggish diffusion kinetics of

G.-Y. Wang, X.-H. Wang, J.-F. Sun*, Y.-M. Zhang,
L.-R. Hou*, C.-Z. Yuan*
School of Materials Science and Engineering, University of Jinan, Jinan 250022, China
e-mail: mse_sunjf@ujn.edu.cn

L.-R. Hou
e-mail: mse_houlr@ujn.edu.cn

C.-Z. Yuan
e-mail: mse_yuancz@ujn.edu.cn; ayuancz@163.com

battery-type electrode materials during insertion/disinsertion is widened, and the above behavior severely hinders the performance of PIHC in terms of rate behavior and long-cycle stability.

To date, a variety of materials such as carbon [7, 8], alloy-based [9], organic compounds [10, 11], and MXene-based materials [12] have been used as the anodes for K^+ storage. Among these anode materials, carbon materials are considered as the most promising candidates due to their low cost, excellent physical/chemical stability, high electrical conductivity and ease of mass production [13]. Coal pitch is an excellent precursor for carbon materials, and its derived soft carbon has adjustable layer spacing. Numerous studies have been reported to prepare pitch-derived soft carbon materials for applications towards K^+ storage [13–15]. Moreover, the rate performance of these soft carbon-based anodes can be promoted by adjusting the morphological structure and porosity, especially, carbon nanofibers (CNF) prepared by electrostatic spinning method have received much attention [16]. If coal pitch was combined with electrostatic spinning, the combination of macroscopic and microscopic effects would be more favorable to the rapid K^+ transport and storage. It is known that the coal pitch is a thermoplastic organic material, which will soften at high temperatures [17]. The oxidation process in air plays an important role in maintaining the morphological structure and chemical properties of thermoplastic organics [18]. However, the low softening point of coal pitch ($\sim$ 180 °C) makes it difficult for coal pitch-based fibers to be stabilized in air. It has become the key issue of how to properly address the stability of coal pitch-based fibers. Unfortunately, there are few relevant studies for this, let alone their applications in PIHC.

In the work, we successfully prepared the coal pitch/polystyrene (PS) fibrous precursor with an electrostatic spinning process from the commercially available low-softening-point coal pitch raw material, which was pre-oxidized with the HNO_3. Then, the porous CNF (PCNF) obtained with simple carbonization and activated PCNF (aPCNF) fabricated with KOH activation were utilized as the anode and cathode materials for the PIHC, respectively. Herein, the reasonable layer spacing, micro/meso-porous synergy and surface pseudocapacitance-dominated storage properties lead to high K^+ storage performance as well as long cycle stability of the PCNF. In particular, the PIHC constructed with aPCNF cathode and PCNF anode achieved high energy/power density and superior cycle stability. Furthermore, this study provides an opportunity to develop a dual-carbon PIHC using low-cost coal chemical waste, thus providing a "waste to treasure" strategy.

2 Experimental

2.1 Synthesis of PCNF

The coal pitch/PS fibers were prepared through the followed process. Briefly, the low-softening-point coal pitch was pre-oxidized using a suitable concentration of HNO_3 for 12 h and then washed to neutral using deionized water and dried in an oven at 60 °C to obtain pre-oxidized coal pitch (denoted as H-pitch). 1.2 g PS was dissolved in a mixture of N, N-dimethylformamide (DMF) and N-methyl-2-pyrrolidone (NMP) at a volume ratio of 1:1 under sonication. 2.4 g (or 0.6, or 1.2 g) H-pitch was added to the above clear solution and stirred overnight. Then, the mixed solution was injected into a syringe. In the electrospinning process, a voltage of 20 kV and a spinning speed of 0.6 ml·h^{-1} were set, receiving the spun fibers by using the aluminum foil at a distance of 20 cm from the needle. After dried overnight in an oven at 60 °C, the electrospun fibers were stabilized in a muffle furnace at 230 °C for 3 h. The resulting product was further annealed at 900 °C for 2 h at a slope of 5 °C·min^{-1} to give the PCNF. The carbon yield of the PCNF was $\sim$ 57.1%.

2.2 Synthesis of aPCNF

The electrospun fibers were pre-oxidized at 230 °C in air at a heating rate of 1 °C·min^{-1} for 3 h and then annealed at 600 °C at a slope of 5 °C·min^{-1} for 2 h to obtain the sample (designed as PCNF-600). Subsequently, the PCNF-600 was ground to a powder and added into a 1.0 mol·L^{-1} KOH solution with a PCNF-600: KOH mass of 1:3 and stirred for 24 h. The mixture was dried to remove the water. Afterwards, the dried PCNF-600/KOH mixture was activated at 900 °C for 3 h in Ar atmosphere. The excess KOH activator by-products in the product were neutralized with 1.0 mol·L^{-1} HCl. The product was then washed with deionized water to pH = 7.0 and dried overnight in a vacuum oven at 80 °C to obtain the aPCNF. The yield of the aPCNF was $\sim$ 12.3%.

2.3 Material characterizations

The obtained samples were characterized by X-ray diffraction (XRD, Rigaku Ultima IV powder X-ray diffractometer with Cu Kα radiation, λ = 0.154056 nm). Morphologies and microstructures of the products were characterized with field-emission scanning electron microscopy (FESEM, JEOL-6300F), transmission electron microscopy (TEM), scanning TEM (STEM), high-resolution TEM (HRTEM, JEM-2100) equipped with energy-

dispersive X-ray spectroscopy (EDS). Micromeritics ASAP 2020 apparatus was used to analyze nitrogen sorption isotherms. Raman spectra were collected using 532 nm excitation on a LAB RAM HR spectrometer. Fourier transform infrared (FT-IR) spectra were performed by using Nicolet iS50 spectrometer with a KBr pellet in the range from 400 to 4000 cm^{-1}.

2.4 Electrochemical measurements

The anodes were prepared by evenly mixing the electroactive material PCNF, acetylene black, and polyvinylidene fluoride (PVDF) binder with a weight ratio of 7:2:1 in NMP. Then, the slurry was coated onto a Cu foil, and dried in a vacuum oven at 80 °C for 12 h. The anodes with a diameter of 12 mm were obtained using a punch machine and the mass loading in each electrode was ∼ 1.2 mg·cm^{-2}. Using the metallic K as the counter/reference electrode, and glass fiber filter (Whatman GF/F) and 0.8 mol·L^{-1} KPF$_6$ dissolved in the ethylene carbonate/dimethyl carbonate mixture (by 1:1 in volume ratio) were used as the separator and electrolyte, respectively. For fabrication of the cathode, PVDF, acetylene black and aPCNF (1:2:7 in weight ratio) in the NMP were mixed, and coated on a fresh Al foil. After dried in vacuum at a temperature of 110 °C, the aPCNF cathode was used to fabricate half-cell configurations and/or full devices in glove box. In order to enhance the stability and minimize the irreversible capacity during the first cycle, the PCNF anode was pre-activated before assembly. To be specific, the PCNF electrode was directly contacted with the metallic potassium in the electrolyte under an extra pressure from glass plates. The weight ratio of the cathode to anode is designed as 3.0 for charge balance. The total mass load of the two electrodes is 3.2–4.0 mg. Both the electrolyte and separator in devices were identical to those applied for the assembly of half cells above. All the electrochemical properties were evaluated by coin cells (CR2032) assembled in an Ar-filled glove box (both O$_2$ and H$_2$O < 0.1 × 10^{-6}). Charge–discharge measurements were conducted on a Land CT2001A battery tester. Cyclic voltammetry (CV) curves and electrochemical impedance were recorded with an electrochemical workstation (Ivium). The energy density (E, Wh·kg^{-1}) and power density (P, W.kg^{-1}) of PIHC were calculated by the following Equations (1–3) [19]:

$$P = \Delta V \times i/m \tag{1}$$

$$E = P \times t/3600 \tag{2}$$

$$\Delta V = (V_{max} + V_{min})/2 \tag{3}$$

where i, t, m, V_{max}, and V_{min} were the discharge current (A), discharge time (s), total mass of electroactive materials in both anode and cathode (kg), voltage at the beginning of discharge (V), and voltage at the end of discharging (V), respectively.

3 Results and discussion

3.1 Preparation and characterization of samples

Firstly, we used HNO$_3$ pre-oxidation method to treat the low-softening-point pitch raw material. Figure S1a, b shows the digital photos before and after the pre-oxidation treatment, respectively. The original coal pitch shows a light brownish-yellow color, while after the HNO$_3$ treatment, the H-pitch turns black in color. The granularity of the powder increases significantly. FT-IR was performed to detect changes in the chemical structure of the coal pitch obtained before and after pre-oxidation. Compared to the original coal pitch, the H-pitch exhibited some significant changes, as shown in Fig. S1c. The peaks near 798, 1350 and 1580 cm^{-1}, which are associated with the –C–N–H or C–H bending planes of the aromatic ring and the –C–H and C–N, aromatic C=C deformations, turn out to be more distinct, and the two new bonds near 1359 and 1528 cm^{-1} are attributed to the –NO$_2$ feature, suggesting that the HNO$_3$ pretreatment undergoes the polymerization and condensation reactions introducing new –NO$_2$ groups. [18, 20].

Schematic diagrams for the synthesis of PCNF and aPCNF samples are shown in Scheme 1. Firstly, in order to explore suitable ratios of spinning solutions, we prepared nanofibers by electrospinning technique from a mixture of H-pitch and PS in different mass ratios (H-pitch: PS = 1:2, 1:1, 2:1) and named them NF-0.5, NF-1 and NF-2, respectively. As shown in Fig. S2a–c, the fibrous protofilaments consist of long, straight, disordered fibrils, indicating the successful preparation of fibrous structures. The air pre-oxidation plays an important role in stabilizing the structure of fibers, especially for thermoplastic organics such as coal pitch [18]. The structure of NF-0.5 collapsed after pre-oxidation and the fiber morphology disappeared (Fig. S2d). This is related to the inability of the very low molecular weight and discontinuous coal pitch to form an effective oxidative cross-linked structure to inhibit the brittle fracture of PS during heat treatment, resulting in the failure to maintain fiber morphology. NF-1 keeps partially the fiber morphology, while NF-2 well remains the fibrous morphology (Fig. S2e, f). It should be ascribed to the fact that the enough coal pitch molecules in NF-2 can cross-link and polymerize with each other during the pre-oxidation stage to ensure the fiber morphology. The fibers prepared from the H-pitch can retain stability in the subsequent air pre-oxidation, no serious fusion and binding of fibers
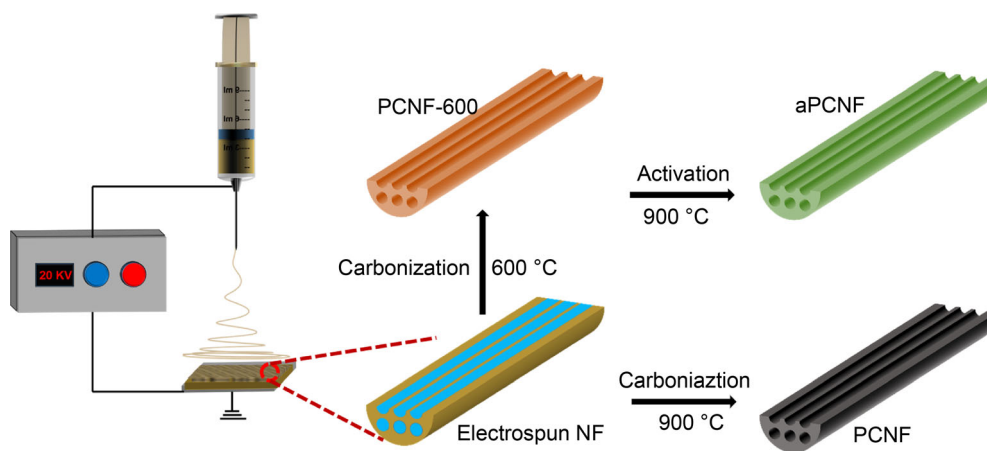
Scheme 1 Synthetic schematic for PCNF and aPCNF

caused by melting of coal pitch during heating occurred, indicating that the melting behavior of coal pitch fibers during air stabilization could be solved by pretreating coal pitch feedstock with HNO_3 [21]. Interestingly, when the pre-oxidation of electrospun fibers in air is completed, the cross-linked structure with an "X-shape" is formed partially at the junction points between some fibers, which is produced by the cross-linked polymerization between the coal pitch molecules in contact with each other during the pre-oxidation stage [22]. Subsequently, PCNF is achieved by simple carbonization of NF-2, while aPCNF was obtained by activating the PCNF-600 with KOH for pore formation.

FESEM and HRTEM measurements were performed to study the microstructure of PCNF and aPCNF samples. As shown in Fig. 1a, after carbonization, PCNF maintains a perfect fiber morphology with diameters mostly in the range of 500–700 nm, and they are randomly stacked to form a three-dimensional (3D) nonwoven network. Further magnified image (Fig. 1b) depicts apparent elongated pores, which are produced by the pyrolysis of PS at high temperatures [23]. TEM studies can provide more detailed information about the pore structure (Fig. 1c, d). TEM images of the obtained PCNF show numerous nanochannels along the PCNF fiber direction with a diameter range of 20–30 nm. The rich pore structure not only increases the specific surface area (SSA) of the material, but also provides more channels for rapid ion transport. The HRTEM image in Fig. 1e shows obvious lattice stripes corresponding to the (002) crystal plane of carbon with a crystal interlayer distance around 0.366 nm, which is much larger than the graphite crystal plane spacing, favoring the
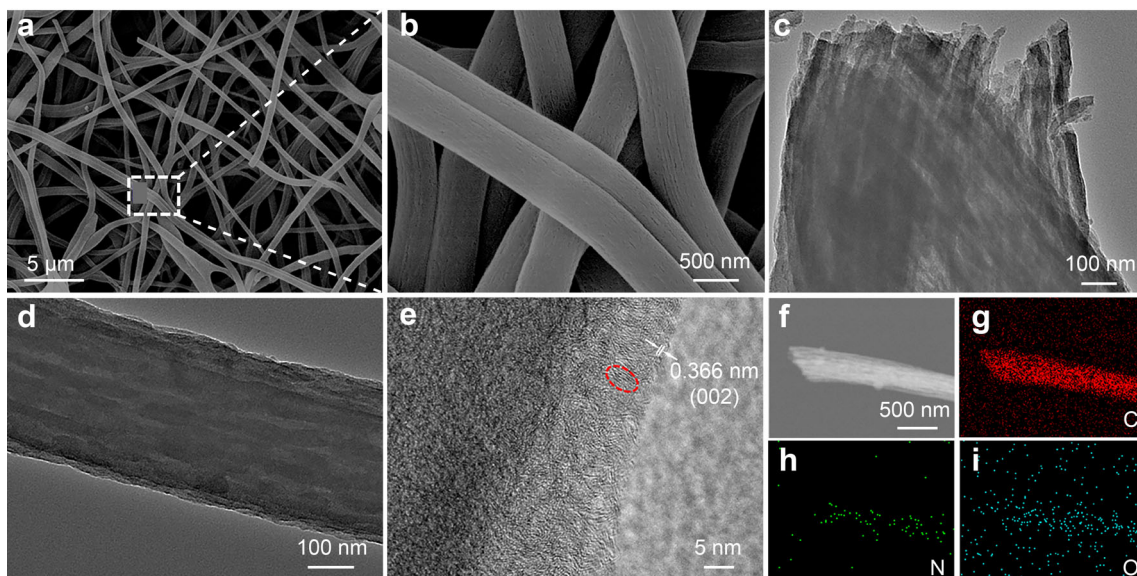

Fig. 1 Morphology characterizations of PCNF: **a**, **b** FESEM images; **c**, **d** TEM images; **e** HRTEM image; **f** STEM image; **g–i** corresponding EDS mapping images

insertion/extraction of K^+ [24]. It should also be noted that the graphitized microcrystals appear in the areas marked in red in the image due to the highly aromatic nature of coal pitch and the tendency to graphitize [25]. It will greatly improve the electrical conductivity and enhance the electron transfer rate of the electrode material, which is beneficial to the rate performance. In addition, the corresponding EDS mapping images of the elemental distributions (Fig. 1f–i) reveal that HNO_3 as well as pre-oxidation allows the doping of N, O in the fiber matrix. As shown in Fig. S3a, b, both PCNF-600 and aPCNF maintain the 3D fiber morphology. Subsequent TEM images of aPCNF (Fig. S3c, d) further confirm the existence of a multi-channel structure, and the stability of the structure may facilitate the construction of PIHC devices with long cycling performance. Further HRTEM image evidences that after KOH activation, the obtained aPCNF exhibits a large number of disordered structures inside due to the etching effect of KOH on the carbon material, meanwhile, the carbon layer spacing also reached 0.401 nm [6]. Corresponding EDS mapping images (Fig. S3f–i) demonstrate that N, O are still doped in the carbon fiber matrix after activation.

The phase structures of PCNF and aPCNF were characterized using XRD. As shown in Fig. 2a, PCNF shows two broad diffraction peaks centered near 24.2° and 43.4° that can be attributed to (002) and (101) diffraction of

carbon, indicating the presence of amorphous carbon material [25]. It is noteworthy that a sharp crystal peak appears at 26.3°, which corresponds to the (002) crystal plane of graphite, in accordance with the TEM observations [25]. Figure S4a shows XRD pattern of aPCNF with two broad peaks centered near 22° (002) and 43.4° (101) clearly pointing to the amorphous carbon material. Meanwhile, the interlayer distance of PCNF and aPCNF is 0.36 and 0.40 nm, respectively, which is higher than that of graphite, as derived from Bragg's law. The increased interlayer distance of the material can be attributed to the doping of heteroatoms such as N, O through HNO_3 treatment and pre-oxidation and the activation of KOH. Raman spectra of the PCNF are shown in Fig. 2b, with two strong characteristic peaks at 1359 and 1603 cm^{-1}, corresponding to D-band (disordered carbon and/or defect-containing graphite structure) and G-band (E_{2g} phonon of sp^2 bonded carbon), respectively [26]. The fitted peak area ratio (I_D/I_G) of the D-band and G-band is used to indicate the degree of graphitization of the material, and the I_D/I_G value of 1.36 for the PCNF indicates that the material contains more defects. Typically, more defects in the PCNF can provide more active sites for K^+ storage, while the presence of graphite microcrystals provides high electrical conductivity for electron transfer.

Figures 2c, S4b reveal the N_2 adsorption–desorption isotherm curves and pore size distributions (built-in plots)
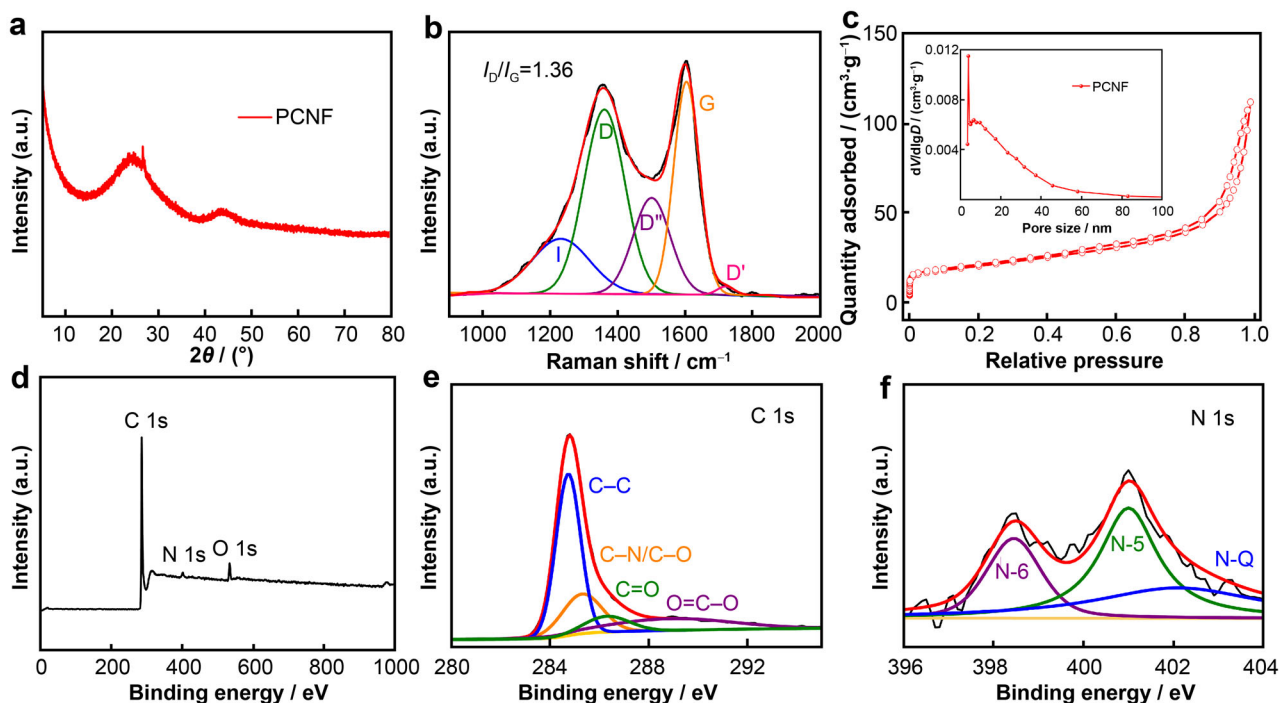

Fig. 2 **a** XRD pattern, **b** Raman spectra, and **c** N_2 adsorption–desorption isotherms and (inset) pore size distribution plot (log differential pore volume versus diameter ($dV/dlgD$) being obtained from mesoporous size analysis based on modified Kelvin equation proposed by Barrett, Joyner and Halenda (BJH)); **d** XPS survey spectrum, high resolution **e** C 1s and **f** N 1s spectra of PCNF

of PCNF and aPCNF, and it can be seen that PCNF exhibits combined characteristics of Types I and IV isotherms [27], whereas aPCNF presents Type I characteristics of isotherms [6]. It can be seen that both two have stratified pores, most of which are microporous and mesoporous. The mesopores of both materials are related to the channels formed after PS pyrolysis [28]. The activation of KOH provides a large number of micropores for aPCNF, and it is generally believed that their main reaction $(2C + 6KOH \rightarrow 2K + 3H_2 + 2K_2CO_3)$ is involved at high temperatures. After that H_2O and CO_2 generated from the intermediate products further react with C to form a large number of pores, which significantly increases the SSA of aPCNF (2169 $m^2 \cdot g^{-1}$), much larger than that of PCNF (63 $m^2 \cdot g^{-1}$) [29]. Also, the metal K formed at high temperature tends to expand the carbon layer spacing of the material, which is verified by XRD analysis above. The combination of mesopores and micropores effectively reduces the ion migration resistance, shortens the ion migration distance, accelerates charge storage, and promotes the K^+ insertion/extraction.

The surface chemical state of PCNF was analyzed using XPS, and the results were well fitted using XPSPEAK41 software, as shown in Fig. 2d–f. Figure 2d clearly reveals the coexistence of C, N and O, indicating the effective doping of N, O after HNO_3 treatment as well as pre-oxidation, which helps to increase the specific capacities of the PCNF electrode. More specifically, the doping of O atoms increases the wettability of carbon material and facilitates the increase of the effective SSA for charge storage [30]. For the C species, the high-resolution C 1s spectrum (Fig. 2e) is fitted to four peaks at $\sim$ 284.7, $\sim$ 285.3, $\sim$ 286.3 and $\sim$ 288.8 eV, attributed to graphitic C–C, C–O/C–N, C=O, and O–C=O chemical bonds, respectively [31]. The spectra in N 1s (Fig. 2f) are reasonably well fitted to pyridine N (i.e., N-6, $\sim$ 398.4 eV), pyrrole N (i.e., N-5, $\sim$ 400.9 eV), and graphite N (i.e., N-Q, $\sim$ 402.3 eV), respectively [6]. The total doping N was estimated to be $\sim$ 2.8 at%. More specifically, N-6 ($\sim$ 0.8 at%) and N-5 ($\sim$ 1.7 at%) are associated with defects and active sites that enhance the surface-controlled pseudocapacitance contribution, promote K^+ diffusion and increase the K^+ storage capacity, especially at high charge/discharge rates. The N-Q ($\sim$ 0.3 at%) facilitates the fast electron transfer in PCNF, thus improving the multiplicative performance [6].

3.2 Electrochemical evaluation of PCNF anode

The electrochemical properties of PCNF were investigated in half cells with potassium metal as the counter electrode. To gain insight into the electrochemical behavior of the PCNF electrode, CV was measured at a scan rate of 0.1 $mV \cdot s^{-1}$ o of 0.01–3.00 V (vs. K/K^+). The specific electrochemical response in the initial three CV cycles is shown in Fig. 3a. In the first discharge cycle, a broad peak starting at 0.92 V can be observed and then disappears in the subsequent cycles, which always corresponds to the irreversible reaction of K^+ with functional groups on the PCNF surface and the formation of the solid electrolyte interface (SEI) [32]. In addition, the sharp cathodic peak at 0.02 V is attributed to the insertion of K^+ into the carbon layer, and the oxidation peak at 0.27 V reveals the extraction of K^+ [32]. After the first cycle, the CV curves are kept well, indicating the good reversibility and stability of PCNF towards K^+ storage.

The selected charge/discharge plots (0.1 $A \cdot g^{-1}$) of the PCNF are shown in Fig. 3b. In the initial discharge/charge process, the specific capacities of the PCNF are estimated as $\sim$ 851.5 and $\sim$ 267.2 $mAh \cdot g^{-1}$, respectively, corresponding to a Coulomb efficiency (CE) value of $\sim$ 30.9%. The low CE value here should be attributed to the formation of the SEI layer and the irreversible reaction of K^+ with the functional groups on the PCNF surface, as evidenced by the above CV curves. In addition, the charge/discharge plots of the third cycle almost overlap with those of the second cycle, indicating that the PCNF has good reversibility during the cycle. Figure 3c shows the rate performance of the PCNF electrode, where the rate performance of the material was further evaluated in the current density range of 0.2–10.0 $A \cdot g^{-1}$ after an initial 10 activation cycles at a current density of 0.1 $A \cdot g^{-1}$. The discharge capacities of the PCNF were estimated to be $\sim$ 227.6, $\sim$ 201.2, $\sim$ 179.8, $\sim$ 157.5, $\sim$ 126.0 and $\sim$ 74.7 $mAh \cdot g^{-1}$ at different current densities of 0.2, 0.5, 1.0, 2.0, 5.0, and 10.0 $A \cdot g^{-1}$, respectively. When the current density rechanges back to 0.1 $A \cdot g^{-1}$, the discharge capacity recovers to 221.2 $mAh \cdot g^{-1}$ once again, indicating its superb electrochemical reversibility and stability. The excellent rate performance is superior to that previously reported for other carbon anodes [15, 33–36], as shown in Fig. 3d.

To further analyze the storage behaviors of K^+ in PCNF electrodes, CV measurements were performed at various scan rates from 0.3 to 2.3 $mV \cdot s^{-1}$. As shown in Figs. 3e, S5a–c. The capacitive effect is qualitatively calculated according to the relationship between the current (i) and scanning rate (v) measured from CV curves: $i = av^b$, in which both a and b are constants. Generally, the a value of 0.5 represents a typical diffusion control process, while the b value extracted from the slope of the lg$i$ vs. lg$v$ plot is 1.0 for the capacitance-based process [37]. Figure S5b shows the lg$i$ versus lg$v$ curves for the cathode and anode peaks. The b value of 0.93 for both the cathode and anode peaks reveals that the K^+-storage behaviors of the PCNF anode stems from the synergistic contributions of the diffusion-controlled intercalation and pseudocapacitive processes
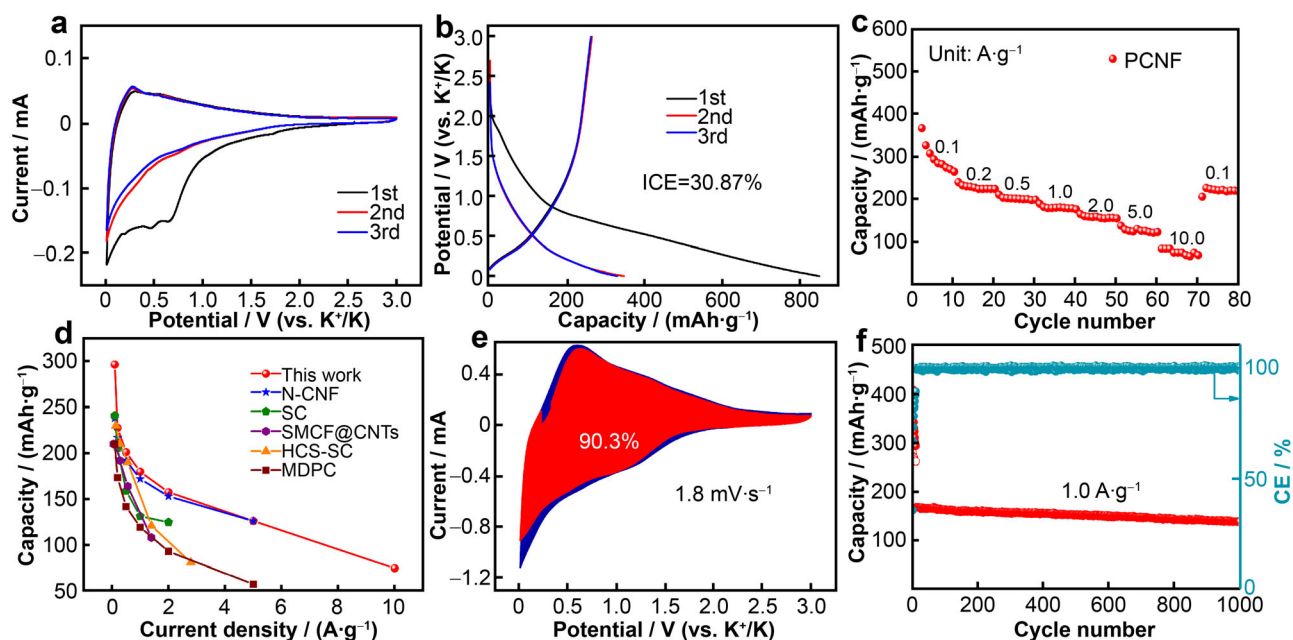
Fig. 3 a Initial three CV curves (0.1 mV·s^{-1}), **b** galvanostatic charge–discharge curves at 0.1 A·g^{-1}, **c** rate capacities, **d** rate performance comparison with latest reported carbon-based anodes, **e** CV curve (1.8 mV·s^{-1}) with pseudocapacitive contribution (red region), and **f** long-time cycling properties at 1.0 A·g^{-1} of PCNF anode

driven by the surface/interface, where the latter dominates the charge storage properties of the PCNF here [37]. The pseudocapacitive contributions at different scanning rates can be distinguished by the equation $i = k_1 v + k_2 v^{1/2}$, where $k_1 v$ and $k_2 v^{1/2}$ represent the current fractions from the capacitance effect and the diffusion control part, respectively [8]. Impressively, the capacitive storage contribution to the total specific capacity increases from 69.5% (0.3 mV·s^{-1}) to an impressive value of 93.8% (2.3 mV·s^{-1}). As the scanning rate increases, the capacitance contribution is enhanced accordingly, which again proves that the storage mechanism of PCNF anodes mainly involves surface capacitance processes. This will be favorable to the rate capacity and cyclic stability of the electrodes at high current density [8]. To further analyze the behavior of PCNF in kinetics, we performed electrochemical impedance tests on the newly assembled half cells, and the results are shown in Fig. S5d. The electrochemical impedance profile consists of a half circle and a diagonal line. The semicircle in the high-frequency region represents the charge transfer resistance between the electrolyte and the electrode material, and the diagonal line in the low-frequency region represents the ion diffusion resistance [14]. We observe from Fig. S5d that the charge transfer resistance (R_{ct}) of the PCNF is 546.8 Ω. Similarly, the slope in the low frequency region is significantly greater than 45°, and the higher slope corresponds to a faster ion transport rate in the electrode [14]. It can be concluded that the multi-channel fibrous structure brings a

larger contact area between the active substance and the electrolyte while accelerating the K$^+$ transport rate. Figure 3f shows the cycling performance and corresponding CE data of the PCNF electrode at a high current density of 1.0 A·g^{-1} after activation for 5 cycles at 0.1 A·g^{-1}. The PCNF electrode maintains a discharge capacity of ∼ 140 mAh·g^{-1} and a high CE of ∼ 100% after 1000 cycles. The rational pore structure, 3D conductive network, and large layer spacing endow the PCNF anode with excellent rate and cycling performance for efficient K$^+$ storage.

3.3 Electrochemical evaluation of aPCNF electrode

Compared with commercially available activated carbon (AC), the use of cathodes and anodes derived from a single precursor source can solve the problem of material mismatch between battery-type anodes and capacitor-type cathodes. We obtained aPCNF using KOH activation pore-making treatment. The electrochemical properties of the aPCNF samples were tested in a half-cell configuration within a voltage window of 2.0–4.0 V. Compared with PCNF, aPCNF has a large SSA, coupled with an abundant micro/mesoporous structure due to the activation of KOH. The open porous structure allows efficient access of electrolyte ions to the active surface of the electrode material and provides more active sites/defects to facilitate the adsorption and transport of electrolyte ions during rapid charge/discharge. As shown in Fig. S6a, b, the CV profiles
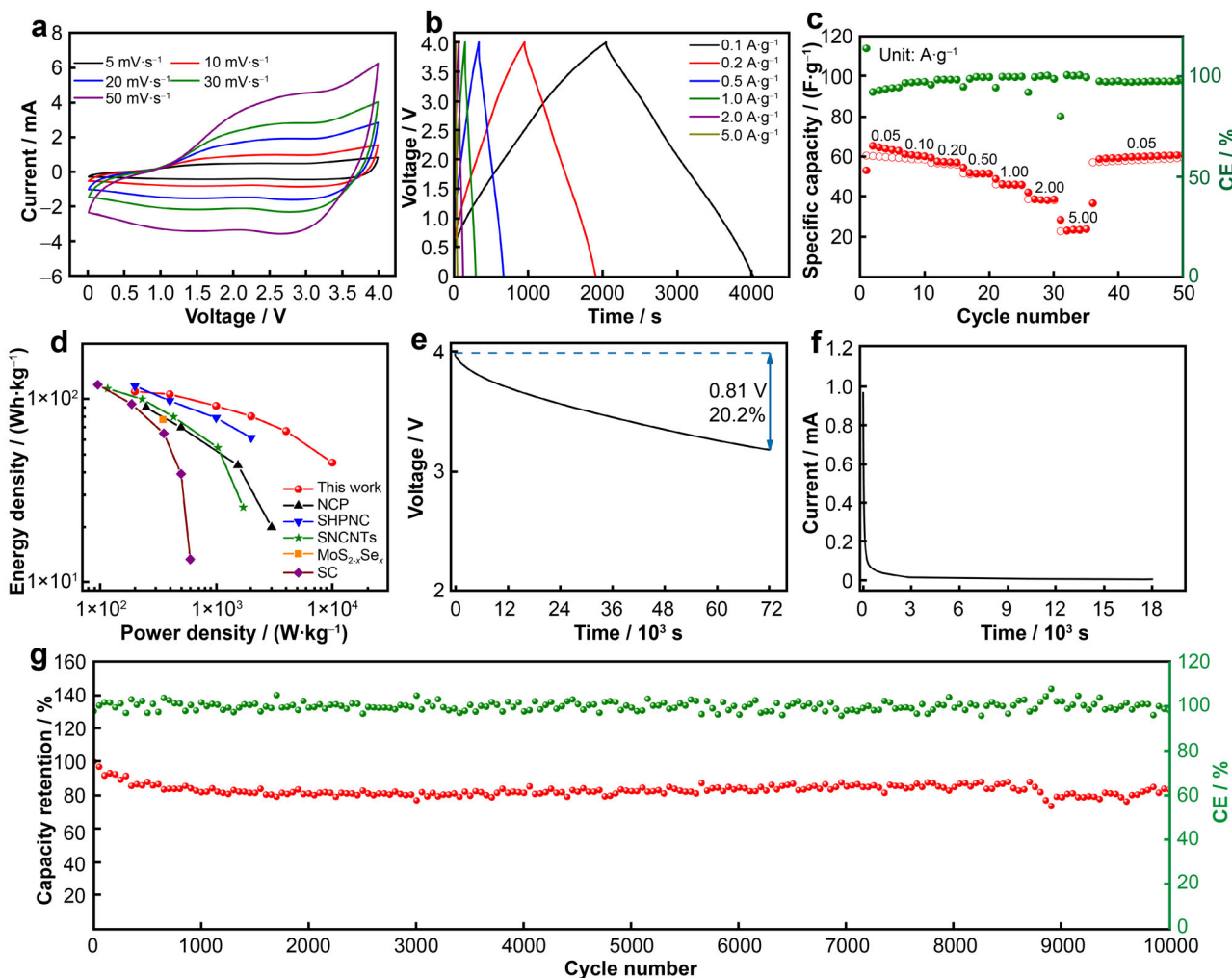
Fig. 4 Electrochemical performance of PCNF//aPCNF PIHC: **a** CV curves at different scan rates, **b** charge–discharge plots at 0.1–5.0 A·g^{-1}, **c** rate performance, **d** Ragone plots compared with other PIHCs, **e** self-discharge plot, **f** leakage current plot, and **g** long-term cycling performance at 1.0 A·g^{-1}

under different scan rates have no obvious redox peaks, and the corresponding charge/discharge curves are almost straight lines, showing the typical capacitive feature of the aPCNF [6]. Figure. S6c shows the specific capacity of the aPCNF electrode as a function of current density. At a current density of 0.1 A·g^{-1}, the specific capacity of aPCNF electrode reaches 62.8 mAh·g^{-1}, and even at a high current density of 1.0 A·g^{-1}, a specific capacity of 51.8 mAh·g^{-1} is still achieved, significantly higher than that of AC electrode. This indicates that aPCNF is an ideal capacitive cathode material for PIHC.

3.4 Electrochemical properties of PCNF//aPCNF PIHC

The excellent electrochemical properties of PCNF and aPCNF electrodes in terms of capacity, rate performance and long-cycle stability are well suited for their application

in PIHC. We use pre-activated PCNF as a high-power anode and aPCNF as a high-energy cathode to construct the PIHC devices. The mass ratio of PCNF to aPCNF was reasonably fixed at 1.0: 3.0 to meet the capacity matching of the two related electrodes [38, 39]. The electrochemical performance of PIHC was tested in the voltage range of 0.01–4.00 V [40, 41]. Figure 4a shows CV curves of the assembled PIHC at different scan rates (5.0–50.0 mV·s^{-1}). It can be seen that all CV curves show a slightly deviated rectangular shape at different scan rates, which remains well with scan rates increasing. Meanwhile, the approximately symmetric triangles of the constant-current charge/discharge plots (Fig. 4b) confirm the characteristic capacitive properties of the device in the current density range from 0.1 to 5.0 A·g^{-1} [42]. As shown in Fig. 4c, the specific capacitances are ∼ 61.9, ∼ 60.9, ∼ 57.6, ∼ 52.1, ∼ 46.5, ∼ 39.1 and ∼ 24.4 F·g^{-1} at different current densities of 0.05, 0.10, 0.20, 0.50, 1.00, 2.00 and 5.00

A·g^{-1}, respectively. When the current density returns to 0.05 A·g^{-1}, the specific capacitance reverts to ∼ 54.1 F·g^{-1}, showing anomalous electrochemical reversibility and fast kinetic behavior. To further illustrate the high energy and high-power characteristics, Ragone plots are profiled as shown in Fig. 4d. Specifically, the device can deliver an energy density of up to 110.0 Wh·kg^{-1} at a power density output of 200.0 W·kg^{-1}. Even at extremely high-power densities of 10,000 W·kg^{-1}, the device is able to maintain an impressive energy density of 45.0 Wh·kg^{-1}. The PIHC device based on the all-carbon electrodes shows more competitive electrochemical performance compared to other reported devices [5, 43–46], as summarized in Fig. 4d. Figure 4e shows the self-discharge profile of the whole PIHC device. Apparently, after fully charged to 4.0 V at a current density of 0.1 A·g^{-1}, the open-circuit voltage of the device drops by 0.81 V after 20 h, which corresponds to a voltage loss of only ∼ 20.2%. More strikingly, after 10,000 consecutive charge/discharge cycles, the capacity retention is estimated at 83.5% (i.e., 1.65‰ capacity loss per cycle), as well as a high CE value of ∼ 100% during the test. In addition, the leakage current of the PIHC is only 6 μA (Fig. 4f). Figure 4g shows the long cycle characteristics of the PIHC with a current density of 1.0 A·g^{-1}. The extremely low self-discharge allows for effective energy storage and excellent long-cycle stability. These outstanding results prove its broad practical application prospects.

4 Conclusion

In conclusion, in the contribution, we used HNO$_3$ pre-treated coal pitch as raw material to prepare coal pitch derived CNFs precursors using a facile electrostatic spinning technique. Then fibrous carbon materials synthesized by carbonization and KOH activation treatments of the precursors were used to fabricate a high-performance dual-carbon PIHC as anode and cathode electrode, respectively. Benefiting from the rational micro/mesoporous structure, continuous 3D conductive network, graphical microcrystals, and the dominant surface pseudocapacitance contribution conferred excellent rate and cycling performance of the PCNF. Meanwhile, the aPCNF cathode exhibited a high SSA of 2169 m^2·g^{-1}. The rich aperture structure with continuous electron transfer path rendered the aPCNF with excellent capacitive performance. Taking advantage of the PCNF anode and aPCNF cathode, the constructed PCNF// aPCNF PIHC devices exhibited superb energy density (∼ 110.0 Wh·kg^{-1} at 200.0 W·kg^{-1}), attractive capacitance retention (∼ 83.5% capacity retention after 10,000 cycles at 1.0 A·g^{-1}), small leakage current (∼ 6 μA), and moderate self-discharge capability (∼ 20.2% voltage loss

after 20 h). The similar electrochemical rate behaviors of the unique dual-carbon electrodes overcome the kinetic mismatch towards the advanced PIHC, providing a new way to prepare high-performance ionic capacitors for the practical applications.

Declarations

Conflict of interests The authors declare that they have no conflict of interest.

References

[1] Li GC, Yang ZW, Yin ZL, Guo HJ, Wang ZX, Yan GC, Liu Y, Li LJ, Wang JX. Non-aqueous dual-carbon lithium-ion capacitors: a review. J Mater Chem A. 2019;7(26):15541. https://doi.org/10.1039/C9TA01246J.

[2] Chang XQ, Zhou XL, Ou XW, Lee CS, Zhou JW, Tang YB. Ultrahigh nitrogen doping of carbon nanosheets for high capacity and long cycling potassium ion storage. Adv Energy Mater. 2019;9(47):1902672. https://doi.org/10.1002/aenm.201902672.

[3] Nagamuthu S, Zhang YM, Xu Y, Sun JF, Zaman FU, Denis DK, Hou LR, Yuan CZ. Non-lithium-based metal ion capacitors: recent advances and perspectives. J Mater Chem A. 2022;10(2):357. https://doi.org/10.1039/D1TA09119K.

[4] Xu J, Dou SM, Cui XY, Liu WD, Zhang ZC, Deng YD, Hu WB, Chen YN. Potassium-based electrochemical energy storage devices: development status and future prospect. Energy Storage Mater. 2021;34:85. https://doi.org/10.1016/j.ensm.2020.09.001.

[5] Wang F, Liu Y, Wei HJ, Wei HJ, Li TF, Xiong XH, Wei SZ, Ren FZ, Alex AV. Recent advances and perspective in metal coordination materials-based electrode materials for potassium-ion batteries. Rare Met. 2021;40(2):448. https://doi.org/10.1007/s12598-020-01649-1.

[6] Yang BJ, Chen JT, Liu LY, Ma PJ, Liu B, Lang JW, Tang Y, Yan XB. 3D nitrogen-doped framework carbon for high-performance potassium ion hybrid capacitor. Energy Storage Mater. 2019;23:522. https://doi.org/10.1016/j.ensm.2019.04.008.

[7] Wang D, Tian KH, Wang J, Wang ZY, Luo SH, Liu YG, Wang Q, Zhang YH, Hao AM, Yi TF. Sulfur-doped 3D hierarchical porous carbon network toward excellent potassium-ion storage performance. Rare Met. 2021;40:2464. https://doi.org/10.1007/s12598-021-01715-2.

[8] Sun YW, Wang HL, Wei WR, Zheng YL, Tao L, Wang YX, Huang MH, Shi J, Shi ZC, Mitlin D. Sulfur-rich graphene nanoboxes with ultra-high potassiation capacity at fast charge: storage mechanisms and device performance. ACS Nano. 2021;15(1):1652. https://doi.org/10.1021/acsnano.0c09290.

[9] Sun ZH, Liu Y, Ye W, Zhang J, Wang Y, Lin Y, Hou LR, Wang MS, Yuan CZ. Unveiling intrinsic potassium storage behaviors of hierarchical nano Bi@N-doped carbon nanocages framework via in situ characterizations. Angew Chem Int Ed. 2021;60(13):7180. https://doi.org/10.1002/anie.202016082.

[10] Han PY, Liu FS, Zhang YM, Wang YY, Qin GH, Hou LR, Yuan CZ. Organic-inorganic hybridization engineering of polyperylenediimide cathodes for efficient potassium storage. Angew Chem Int Ed. 2021;60(44):23596. https://doi.org/10.1002/anie.202110261.

[11] Tian HL, Jiang MJ, Hai YL, Wang K, Yang CL, Zhong GH. Nitrogen containing organics: a promising high capacity anode for potassium ion batteries. J Phys Chem Solids. 2022;161:110415. https://doi.org/10.1016/j.jpcs.2021.110415.

[12] Ming FW, Liang HF, Zhang WL, Ming J, Lei YJ, Emwas AH, Alshareef HN. Porous MXenes enable high performance potassium ion capacitors. Nano Energy. 2019;62:853. https://doi.org/10.1016/j.nanoen.2019.06.013.

[13] Lin CR, Wang YJ, Zhong FL, Yu HL, Yan YR, Wu SP. Carbon materials for high-performance potassium-ion energy-storage devices. Chem Eng J. 2021;407:126991. https://doi.org/10.1016/j.cej.2020.126991.

[14] Ma XQ, Xiao N, Xiao J, Song XD, Guo HD, Wang YP, Zhao SJ, Zhong YD, Qiu JS. Nitrogen and phosphorus dual-doped porous carbons for high-rate potassium ion batteries. Carbon. 2021;179:33. https://doi.org/10.1016/j.carbon.2021.03.067.

[15] Wang MY, Zhu YY, Zhang Y, Duan JY, Wang KK, Wang R, Sun GY, Wang CY. Isotropic high softening point petroleum pitch-based carbon as anode for high-performance potassium-ion batteries. J Power Sources. 2021;481:228902. https://doi.org/10.1016/j.jpowsour.2020.228902.

[16] Yan RY, Josef E, Huang HJ, Leus K, Niederberger M, Hofmann JP, Walczak R, Antonietti M, Oschatz M. Understanding the charge storage mechanism to achieve high capacity and fast ion storage in sodium-ion capacitor anodes by using electrospun nitrogen-doped carbon fibers. Adv Funct Mater. 2019;29(26):1902858. https://doi.org/10.1002/adfm.201902858.

[17] Han J, Chae JS, Kim JC, Roh KC. Facile preparation of composite electrodes for supercapacitors by CNT entrapment into carbon matrix derived from pitch at a softening point. Carbon. 2020;163:402. https://doi.org/10.1016/j.carbon.2020.03.033.

[18] Li X, Tian XD, Yang T, He YT, Liu WH, Song Y, Liu ZJ. Coal liquefaction residues based carbon nanofibers film prepared by electrospinning: an effective approach to coal waste management. ACS Sustainable Chem Eng. 2019;7(6):5742. https://doi.org/10.1021/acssuschemeng.8b05210.

[19] Qin L, Liu Y, Zhu SH, Wu DX, Wang GY, Zhang JY, Wang YY, Hou LR, Yuan CZ. Formation and operating mechanisms of single-crystalline perovskite NaNbO$_3$ nanocubes/few-layered Nb$_2$CT$_x$ MXene hybrids towards Li-ion capacitors. J Mater Chem A. 2021;9(36):20405. https://doi.org/10.1039/D1TA03684J.

[20] Tian XD, He YT, Song Y, Yang T, Li X, Liu ZJ. Flexible cross-linked electrospun carbon nanofiber mats derived from pitch as dual-functional materials for supercapacitors. Energy Fuels. 2020;34(11):14975. https://doi.org/10.1021/acs.energyfuels.0c02847.

[21] Vilaplana-Ortego E, Alcañiz-Monge J, Cazorla-Amorós D, Linares-Solano A. Stabilisation of low softening point petroleum pitch fibres by HNO$_3$. Carbon. 2003;41(5):1001. https://doi.org/10.1016/S0008-6223(02)00428-1.

[22] Yuan GM, Li XK, Xiong XQ, Dong ZJ, Westwood A, Li BL, Ye C, Ma GZ, Cui ZW, Cong Y, Zhang J, Li YJ. A comprehensive study on the oxidative stabilization of mesophase pitch-based tape-shaped thick fibers with oxygen. Carbon. 2017;115:59. https://doi.org/10.1016/j.carbon.2016.12.040.

[23] Liu JY, Xiong ZB, Wang SP, Cai WH, Yang JM, Zhang HX. Structure and electrochemistry comparison of electrospun porous carbon nanofibers for capacitive deionization. Electrochim Acta. 2016;210:171. https://doi.org/10.1016/j.electacta.2016.05.133.

[24] Zhang C, Liu X, Li Z, Zhang CY, Chen ZW, Pan DY, Wu MH. Nitrogen-doped accordion-like soft carbon anodes with exposed hierarchical pores for advanced potassium-ion hybrid capacitors. Adv Funct Mater. 2021;31(23):2101470. https://doi.org/10.1002/adfm.202101470.

[25] Li XW, Sun JY, Zhao WX, Lai YJ, Yu X, Liu Y. Intergrowth of graphite-like crystals in hard carbon for highly reversible Na-ion storage. Adv Funct Mater. 2022;32(2):2106980. https://doi.org/10.1002/adfm.202106980.

[26] Hu XD, Sun XH, Yoo SJ, Evanko B, Fan FR, Cai S, Zheng CM, Hu WB, Stucky GD. Nitrogen-rich hierarchically porous carbon as a high-rate anode material with ultra-stable cyclability and high capacity for capacitive sodium-ion batteries. Nano Energy. 2019;56:828. https://doi.org/10.1016/j.nanoen.2018.11.081.

[27] Li KX, Li P, Sun ZN, Shi J, Huang MH, Chen JW, Liu S, Shi ZC, Wang HL. All-cellulose-based quasi-solid-state supercapacitor with nitrogen and boron dual-doped carbon electrodes exhibiting high energy density and excellent cyclic stability. Green Energy Environ. 2022. https://doi.org/10.1016/j.gee.2022.01.002.

[28] Wang CS, Yan B, Zheng JJ, Feng L, Chen ZZ, Zhang Q, Liao T, Chen JY, Jiang SH, Du C, He SJ. Recent progress in template-assisted synthesis of porous carbons for supercapacitors. Adv Powder Mater. 2021. https://doi.org/10.1016/j.apmate.2021.11.005.

[29] Wang JC, Kaskel S. KOH activation of carbon-based materials for energy storage. J Mater Chem. 2012;22(45):23710. https://doi.org/10.1039/C2JM34066F.

[30] Yang JL, Ju ZC, Jiang Y, Xing Z, Xi BJ, Feng JK, Xiong SL. Enhanced capacity and rate capability of nitrogen/oxygen dual-doped hard carbon in capacitive potassium-ion storage. Adv Mater. 2018;30(4):1700104. https://doi.org/10.1002/adma.201700104.

[31] Li X, Sun N, Tian XD, Yang T, Song Y, Xu B, Liu ZJ. Electrospun coal liquefaction residues/polyacrylonitrile composite carbon nanofiber nonwoven fabrics as high-performance electrodes for lithium/potassium batteries. Energy Fuels. 2020;34(2):2445. https://doi.org/10.1021/acs.energyfuels.9b03637.

[32] Cao B, Zhang Q, Liu H, Xu B, Zhang SL, Zhou TF, Mao JF, Pang WK, Guo ZP, Li A, Zhou JS, Chen XH, Song HH. Graphitic carbon nanocage as a stable and high power anode for potassium-ion batteries. Adv Energy Mater. 2018;8(25):1801149. https://doi.org/10.1002/aenm.201801149.

[33] Xu Y, Zhang CL, Zhou M, Fu Q, Zhao CX, Wu MH, Lei Y. Highly nitrogen doped carbon nanofibers with superior rate capability and cyclability for potassium ion batteries. Nat Commun. 2018;9:1720. https://doi.org/10.1038/s41467-018-04190-z.

[34] Shen C, Yuan K, Tian T, Bai M, Wang JG, Li X, Xie K, Fu QG, Wei B. Flexible sub-micro carbon fiber@CNTs as anodes for potassium-ion batteries. ACS Appl Mater Interfaces. 2019;11(5):5015. https://doi.org/10.1021/acsami.8b18834.

[35] Jian ZL, Hwang S, Li ZF, Hernandez AS, Wang XF, Xing ZY, Su D, Ji XL. Hard-soft composite carbon as a long-cycling and high-rate anode for potassium-ion batteries. Adv Funct Mater. 2017;27(26):1700324. https://doi.org/10.1002/adfm.201700324.

[36] Shao MJ, Li CX, Li T, Zhao H, Yu WQ, Wang RT, Zhang J, Yin LW. Pushing the energy output and cycling lifespan of potassium-ion capacitor to high level through metal-organic framework derived porous carbon microsheets anode. Adv Funct Mater. 2020;30(51):2006561. https://doi.org/10.1002/adfm.202006561.

[37] Tao L, Yang YP, Wang HL, Zheng YL, Hao HC, Song WP, Shi J, Huang MH, Mitlin D. Sulfur-nitrogen rich carbon as stable high capacity potassium ion battery anode: performance

and storage mechanisms. Energy Storage Mater. 2020;27:212. https://doi.org/10.1016/j.ensm.2020.02.004.

[38] Sun CK, Zhang X, Li C, Wang K, Sun XZ, Ma YW. A presodiation strategy with high efficiency by utilizing low-price and eco-friendly Na_2CO_3 as the sacrificial salt towards high-performance pouch sodium-ion capacitors. J Power Sources. 2021; 515:230628. https://doi.org/10.1016/j.jpowsour.2021.230628.

[39] Sun CK, Zhang X, Li C, Wang K, Sun XZ, Liu FY, Wu ZS, Ma YW. A safe, low-cost and high-efficiency presodiation strategy for pouch-type sodium-ion capacitors with high energy density. J Energy Chem. 2022;64:442. https://doi.org/10.1016/j.jechem.2021.05.010.

[40] Pham HD, Fernando JFS, Horn M, MacLeod J, Motta N, Doherty WOS, Payne A, Nanjundan AK, Golberg D, Dubal D. Multi-heteroatom doped nanocarbons for high performance double carbon potassium ion capacitor. Electrochim Acta. 2021; 389:138717. https://doi.org/10.1016/j.electacta.2021.138717.

[41] Qin L, Liu Y, Xu SY, Wang SC, Sun X, Zhu SH, Hou LR, Yuan CZ. In-plane assembled single-crystalline $T-Nb_2O_5$ nanorods derived from few-layered Nb_2CT_x MXene nanosheets for advanced Li-ion capacitors. Small Methods. 2020;4(12): 2000630. https://doi.org/10.1002/smtd.202000630.

[42] El-Khodary SA, Subburam G, Zou BB, Wang J, Qiu JX, Liu XH, Ng DHL, Wang S, Lian JB. Mesoporous silica anchored on reduced graphene oxide nanocomposite as anode for superior lithium-ion capacitor. Rare Met. 2022;41(2):368. https://doi.org/10.1007/s12598-021-01788-z.

[43] Liu MQ, Chang LM, Wang J, Li JH, Jiang JM, Pang G, Wang HR, Nie P, Zhao CM, Xu TH, Wang LM. Hierarchical N-doped carbon nanosheets submicrospheres enable superior electrochemical properties for potassium ion capacitors. J Power Sources. 2020;469:228415. https://doi.org/10.1016/j.jpowsour.2020.228415.

[44] Li XQ, Chen MX, Wang L, Xu HJ, Zhong J, Zhang M, Wang YY, Zhang QS, Mei L, Wang T, Zhu J, Lu BA, Duan XD. Nitrogen-doped carbon nanotubes as an anode for a highly robust potassium-ion hybrid capacitor. Nanoscale Horiz. 2020;5(12):1586. https://doi.org/10.1039/D0NH00451K.

[45] Gao JY, Wang GR, Liu Y, Li J, Peng B, Jiao SH, Zeng SY, Zhang GQ. Ternary molybdenum sulfoselenide based hybrid nanotubes boost potassium-ion diffusion kinetics for high energy/power hybrid capacitors. J Mater Chem A. 2020;8(28): 13946. https://doi.org/10.1039/D0TA01786H.

[46] Fan L, Lin KR, Wang J, Ma RF, Lu BA. A nonaqueous potassium-based battery-supercapacitor hybrid device. Adv Mater. 2018;30(20):1800804. https://doi.org/10.1002/adma.201800804.